

---

# Part II

Measurements and applications



---

## Chapter 8

# Experimental approaches for probing heat transfer and energy conversion at the atomic and molecular scales

**Longji Cui, Edgar Meyhofer and Pramod Reddy**

Recent work has achieved tremendous progress toward experimentally probing energy transport at the nanoscale. In examining the limits of the applicability of classical laws, atomic- and molecular-scale structures have emerged as paradigmatic systems and have revealed exotic transport phenomena that arise in the quantum regime. Moreover, understanding how thermal energy is transported, converted and dissipated at the most fundamental level is of great importance for achieving high-performance energy conversion technologies and rationally designing thermally robust circuits when approaching the limit of electronic miniaturization. In this chapter, we present a brief review of the basic concepts and experimental progress made in atomic- and molecular-scale thermal science. In particular, we focus on the recent development of high-resolution scanning thermal microscopy probes and their applications in understanding heat conduction in atomic and single-molecule junctions as well as thermoelectric energy conversion and heat dissipation in molecular junctions.

### 8.1 Introduction

Atomic-sized structures such as atomic junctions, gaps and molecular chains represent the ultimate limit for the miniaturization of physical devices. Over the past half century, the modern electronics industry has been significantly advanced by the growing demand for faster, larger, and more affordable storage and computing hardware. The physical size of functional units such as transistors has continuously shrunk over the last few decades, approaching the physically allowed size limit—the atomic scale. Whereas classical laws have proven to be useful in describing energy transport phenomena in macroscopic devices and materials, the laws governing transport at the atomic scale remain largely unexplored. The study of energy

transport at the atomic scale provides unique opportunities to test widely accepted rules and frameworks and holds great promise to strongly affect a wide range of contemporary technologies ranging from electronics and photonics to chemical catalysis and energy conversion. To date, a large amount of theoretical and experimental work has been directed toward understanding the electrical transport properties and mechanisms in atomic-sized structures and devices [1, 2]. Although essential for the functionalities and performance of materials, the thermal transport properties of materials and devices ranging in size from a few nanometers (comparable to the characteristic size of the smallest commercially available transistors) down to the single-atom limit have remained largely unexplored. This is due to the fact that, at this length scale, thermophysical properties such as heat flow rates, temperature and energy conversion are quite challenging to measure. Developing novel experimental techniques and approaches to enable quantitative calibration of these critical characteristics remains a key challenge in the field of atomic-scale thermal science.

In this chapter, we focus on reviewing the current state-of-the-art in thermal energy transfer and conversion at the atomic scale. Specifically, we first introduce in section 8.2 some basic concepts of energy transfer and conversion in nano- and mesoscopic devices. From sections 8.3 to 8.6, we review the recent development of scanning thermal microscopy probes and the experimental work that has revealed quantum thermal transport in single-atom junctions, heat dissipation in single-molecule junctions, the observation of the Peltier effect in molecular junctions, and the recent experimental advance enabling the first measurement of thermal conductance of single-molecule junctions. Finally, we conclude this chapter by highlighting some open challenges in this field.

## 8.2 Theoretical concepts

### 8.2.1 Energy transport in atomic-scale junctions

Atomic junctions refer to functional devices with one or a few atoms bridging two electrodes (figure 8.1(a)). Similarly, individual molecules can form molecular junctions by connecting two electrodes through chemical and physical bonds (figure 8.1(b)). For these atomic-sized devices, energy transport via basic energy carriers such as electrons and phonons is often described using Landauer’s quantum transport framework [3–5]. Specifically, when applying a voltage bias ( $V$ ) across atomic-scale junctions, the resultant electrical current ( $I$ ) is given by [6]

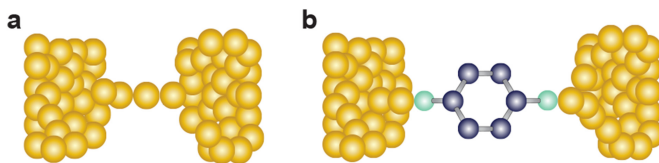


**Figure 8.1.** Schematics of the atomic-sized structures discussed in this chapter. (a) An atomic junction is formed when a one-atom or few-atom wide wire is sandwiched between two macroscopic electrodes. (b) A single-molecule junction.

$$I = \frac{2e}{h} \int_{-\infty}^{+\infty} (f_L - f_R) \tau(E) dE, \quad (8.1)$$

where  $e$  and  $h$  are the electron charge and Planck's constant,  $f_L$  and  $f_R$  are the Fermi–Dirac distributions of the left and right electrodes, respectively, and  $\tau(E)$  is the transmission function, which describes the energy-dependent transmission probability of electrons through the junction. For the specific atomic structures,  $\tau(E)$  can be estimated by employing density functional theory in conjunction with non-equilibrium Green's function techniques [7].

In the approximation of a small bias voltage and low temperatures, equation (8.1) can be further reduced to

$$G_e = \frac{I}{V} = \frac{2e^2}{h} \tau_{E=E_F}, \quad (8.2)$$

where  $G_e$  is the electrical conductance of the junction,  $E_F$  is the Fermi energy of the electrodes and  $\tau_{E=E_F}$  is the transmission probability of all contributing electronic channels (modes) in the junction. Under the circumstance that  $\tau_{E=E_F} = 1$ , which indicates the existence of one fully transparent ballistic channel for electron transport, the electrical conductance is quantized and is given by  $G_e = G_0 = 2e^2/h = 1/(12.9 \text{ k}\Omega)$ .

Thermal energy transport at the atomic scale can also be readily described using the Landauer formalism. Basically, when a temperature difference ( $\Delta T$ ) is applied across the atomic-sized junction, a corresponding heat current flows through the junction, driven by both electrons and phonons. The electronic heat current ( $J_{\text{el}}$ ) and the phononic heat current ( $J_{\text{ph}}$ ) are given by [4, 8]

$$J_{\text{el}} = \frac{2}{h} \int_{-\infty}^{\infty} (E - E_F) \tau(E) (f_L - f_R) dE \quad (8.3)$$

and

$$J_{\text{ph}} = \int_0^{\infty} (h\omega) \tau_{\text{ph}}(\omega) (b_L - b_R) d\omega, \quad (8.4)$$

where  $\omega$  is the phonon frequency,  $\tau_{\text{ph}}(\omega)$  is the energy-dependent transmission function for phonons, and  $b_L$  and  $b_R$  are the Bose–Einstein distributions for the left and the right thermal reservoirs, respectively.

Interestingly, a thermal analog of the quantized electrical conductance can also be derived from equations (8.3) and (8.4) for atomic-scale heat conduction. For ideal thermal coupling between the ballistic atomic conductor and the thermal reservoirs, which results in a transmission probability equaling unity for a single channel, both electronic and phononic contributions to thermal transport are given by

$$G_{\text{th}}^{\text{el}} = G_{\text{th}}^{\text{ph}} = g_0 = \frac{\pi^2 k_B^2 T}{3h}, \quad (8.5)$$

where  $G_{\text{th}}^{\text{el}} = J_{\text{el}}/\Delta T$  and  $G_{\text{th}}^{\text{ph}} = J_{\text{ph}}/\Delta T$  are the electronic and phononic thermal conductances of the atomic junctions, respectively,  $k_{\text{B}}$  is the Boltzmann constant and  $T$  is the temperature of the thermal reservoirs. Here,  $g_0 = (9.456 \times 10^{-13} \times T) \text{ W/K}$  is the quantized thermal conductance that has an expression independent of any material parameters and particle statistics (universal for bosons, fermions and anions) [9–13]. For fermions specifically, the ratio of the quantized thermal and electrical conductance obeys the Wiedemann–Franz law, which relates the electrical transport and the electronic contribution to thermal transport in a material [14] via

$$\frac{G_{\text{th}}^{\text{el}}}{G_{\text{e}}} = LT, \quad (8.6)$$

where

$$L = \frac{\pi^2 k_{\text{B}}^2}{3e^2}. \quad (8.7)$$

Probing the electron contribution to heat transfer provides a window into the nature of electron transport in a material. While in most conventional metallic materials the Wiedemann–Franz law is found to be valid and provides quantitatively good estimates of electronic contributions, there have been recent observations of strong violations in several quasi-one-dimensional and nanomaterials [15, 16], which if understood may provide additional means for controlling energy conversion and transport in future devices.

### 8.2.2 Heat dissipation and thermoelectric energy conversion in molecular junctions

When an electrical current ( $I$ ) flows across a molecular junction, the electrical energy is converted to other energy forms and is eventually dissipated into heat. To better understand this question in nanoscale devices, one may ask a series of questions: How does the energy conversion happen? What is the efficiency of a specific form of energy conversion? Where does the heat dissipate? In Landauer’s framework which accounts for elastically transported electrons, i.e. when no energy exchange happens inside the molecular region, the heat dissipation in the left and right electrodes  $Q_{\text{L}}$  and  $Q_{\text{R}}$ , respectively, is given by [17, 18]

$$Q_{\text{L}} = \frac{2}{h} \int_{-\infty}^{\infty} (\mu_{\text{L}} - E) \tau(E) (f_{\text{L}} - f_{\text{R}}) dE \quad (8.8)$$

and

$$Q_{\text{R}} = \frac{2}{h} \int_{-\infty}^{\infty} (E - \mu_{\text{R}}) \tau(E) (f_{\text{L}} - f_{\text{R}}) dE, \quad (8.9)$$

where  $\mu_{\text{L/R}}$  represent the chemical potentials of the left/right electrodes, respectively.

The thermoelectric energy conversion properties of molecular junctions can also be described within the Landauer transport framework. The open circuit voltage ( $\Delta V$ ) developed across a molecular or atomic junction in the presence of a

temperature difference ( $\Delta T$ ) enables the estimation of the Seebeck coefficient ( $S$ ) of the junction, which is defined by  $S = -\Delta V/\Delta T$ , and can be related to the electronic transmission characteristics of the molecular junction by [19, 20]

$$S = -\frac{\pi^2 k_B^2 T}{3|e|} \left. \frac{\partial \ln(\tau(E))}{\partial E} \right|_{E=E_F}. \quad (8.10)$$

The sign of the Seebeck coefficient indicates the identity of the dominant charge carrier. Specifically, electron-dominated transport results in a negative Seebeck coefficient, whereas hole-dominated transport results in a positive Seebeck coefficient. Further, it can be seen from equation (8.10) that the magnitude of the Seebeck coefficient is determined by the slope of the transmission function at the Fermi level of the junction.

According to the Thompson relation, the Peltier coefficient ( $\Pi$ ) of the molecular junction can also be related to the Seebeck coefficient by

$$\Pi = TS, \quad (8.11)$$

where  $T$  is the absolute temperature of the junction. The Peltier effect describes the reversible heating and cooling effects that arise when an electric current flows across the isothermal molecular junction.

The thermoelectric energy conversion efficiency of a material is usually described by a quantity called the figure of merit ( $ZT$ ). It is defined as  $ZT = S^2\sigma T/\kappa$ , where  $\sigma$  is the electrical conductivity and  $\kappa$  is the thermal conductivity. The corresponding  $ZT$  of a molecular junction can be defined similarly as

$$ZT = \frac{S^2 G_e T}{G_{th}}, \quad (8.12)$$

where  $G_e$  and  $G_{th}$  represent the electrical and thermal conductances, respectively. Given the temperatures of the left and right electrodes,  $T_L$  and  $T_R$  (assuming  $T_L < T_R$ ), the heat-to-electricity conversion efficiency of molecular junction ( $\eta$ ) is given by

$$\eta = \eta_C \frac{\sqrt{1 + ZT} - 1}{\sqrt{1 + ZT} + T_L/T_R}, \quad (8.13)$$

where  $\eta_C = 1 - T_L/T_R$  is the Carnot efficiency, which gives the highest energy conversion efficiency any heat engine can reach.

### 8.3 Heat transfer and energy conversion at the atomic scale: experiments

Performing thermal transport measurements at the atomic scale is challenging for a number of reasons. First, atomic-scale structures, due to their nanoscale dimensions, cannot be visually accessed using optical microscopy tools. This frustrates efforts to conduct *in situ* observations and manipulations of the studied objects while simultaneously performing transport measurements, for example, using well-

established thermal characterization tools based on optical approaches [21, 22]. Second, the magnitude of heat flow in such structures is exceedingly small, requiring high-resolution thermal sensing techniques to reliably record the signals of interest. In order to overcome these challenges, researchers have developed scanning thermal microscopy (SThM)-based approaches [23–26] where custom-fabricated high-resolution thermal sensors are integrated into scanning probes to achieve a nanowatt or even picowatt (pW) scale heat current resolution. Further, these tools enable reliable creation and manipulation of atomic-sized objects. Below, we present a brief review of the experimental progress made in applying SThM-based techniques to address open questions in atomic-scale thermal science. Specifically, we will focus on recent work on the measurement of the quantum of heat transport in single-atom junctions, heat dissipation in single-molecule junctions, the Peltier cooling in molecular junctions, as well as the measurement of thermal conductance of single alkanedithiol molecule junctions. For a detailed review of the theoretical and experimental progress in these topics, readers are referred to recent literature [27, 28].

### 8.3.1 Quantum heat transport in single-atom junctions

Key to probing heat conduction in atomic junctions is the development of probes that can both enable the creation of atomic junctions and resolve heat flows in such junctions. Recently, calorimetric scanning thermal microscopy (C-SThM) [29] probes, which are indeed capable of achieving the above-described goals, were developed. As shown in figure 8.2, the micro-fabricated probes feature a suspended island that is isolated by long ‘T’ shaped beams that feature a large thermal resistance ( $R_P \sim 1.3 \times 10^6$  K/W). Further, within the suspended island a high-resolution Pt thermometer with a temperature resolution of  $<1$  mK (in a 10 Hz bandwidth) is embedded. These combined characteristics make it possible to measure a thermal conductance variation of  $\sim 25$  pW  $K^{-1}$ , when a temperature difference of  $\sim 20$  K is applied across atomic-scale junctions. Moreover, the two long, T-shaped  $SiN_x$  beams, which are critical for achieving a large thermal resistance, also feature very high stiffness values ( $>10^4$  N  $m^{-1}$  in the normal direction) which greatly reduces thermal fluctuation [26] and enhances the stability of atomic junctions.

In order to probe heat transport, atomic junctions were created by employing approaches similar to those established in past pioneering works [30, 31]. Specifically, an STM break junction technique [32] is employed to stably create and maintain the metallic atomic junctions. Briefly, the Au-coated tip of the C-SThM probe is displaced toward a planar Au substrate by piezoelectric actuation. When Au on the tip makes contact with Au in the substrate the electrical conductance of the junction reduces to a few hundred ohms (i.e. electrical conductance values that are significantly larger than  $G_0$ ). The tip is subsequently slowly withdrawn from the contact (typically at a rate smaller than  $1$  nm  $s^{-1}$ ). During this process, the nanoscale contact region thins continuously by mechanical stretching until the formation of a single-atom junction as established in several past works [32]. A voltage bias and a temperature differential are applied across the tip

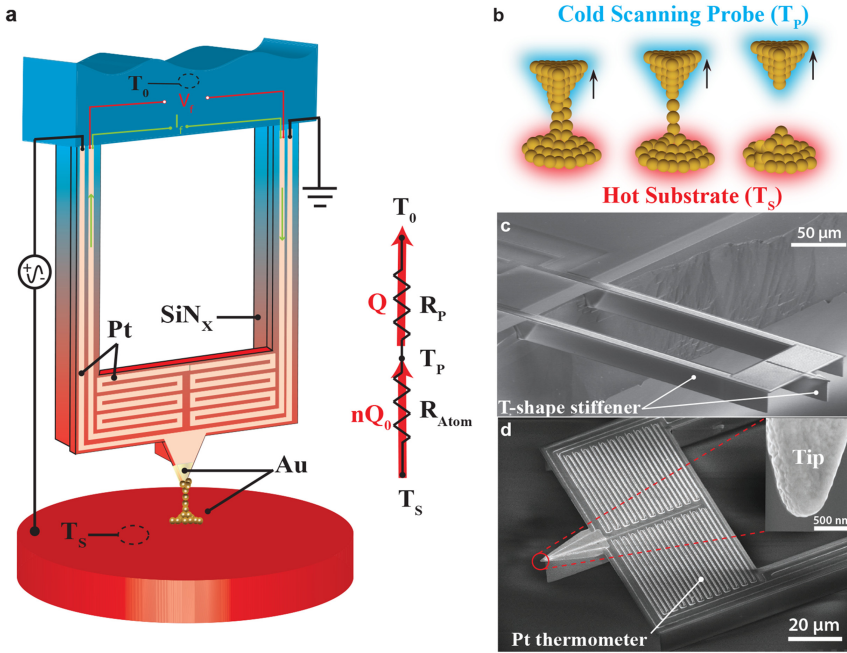


**Figure 8.2.** Experimental set-up and strategy for measuring heat transport in atomic junctions. (a) Schematic of a micro-fabricated C-SThM probe. Simultaneous thermal and electrical transport measurements are performed by monitoring the temperature change of the probe and the tunneling current flowing across the atomic junction, respectively. A resistance network is shown to illustrate the energy flow ( $Q$ ) and relevant thermal resistance in the system, where  $R_P$  and  $R_{\text{Atom}}$  are the thermal resistance of the C-SThM probe and the atomic junction, and  $T_0$ ,  $T_P$  and  $T_S$  correspond to the temperature of the thermal reservoir, the probe and the substrate, respectively. (b) Schematics showing the forming, thinning and breaking of an atomic junction during the withdrawal process of the C-SThM probe from the heated substrate. (c) SEM image (side view) of a C-SThM probe with two long and stiff T-shaped  $\text{SiN}_x$  beams. (d) SEM image (top view) of the probe featuring an Au-coated tip (inset) and an integrated Pt thermometer on the suspended island. Reproduced with permission from [29]. Copyright 2017 American Association for the Advancement of Science.

(at temperature  $T_P$ ) and the substrate (temperature  $T_S$ ) to quantify the electrical conductance and thermal conductance simultaneously. Specifically, the electrical current is measured using a current amplifier connected in series with the junction, while the heat current flowing in or out of the C-SThM probe is quantified by measuring the small temperature change ( $\sim 1$  mK or smaller) of the suspended island ( $\Delta T_P$ ), which is monitored via the integrated Pt thermometer. The thermal conductance of the atomic junctions ( $G_{\text{Th}}$ ) can be related to the temperature change by  $G_{\text{Th}} = \Delta T_P / [R_P(T_S - T_P - \Delta T_P)]$ , where  $R_P$  is the thermal resistance of the probe, and  $T_S$  and  $T_P$  are the temperatures of the substrate and the probe, respectively.

Representative results from electrical and thermal transport measurements on Au atomic junctions are summarized in figure 8.3. It can be seen that, as the separation between the tip and substrate is increased, the electrical and thermal conductances of the junction decrease in steps. It can be seen that the steps are found to favor values

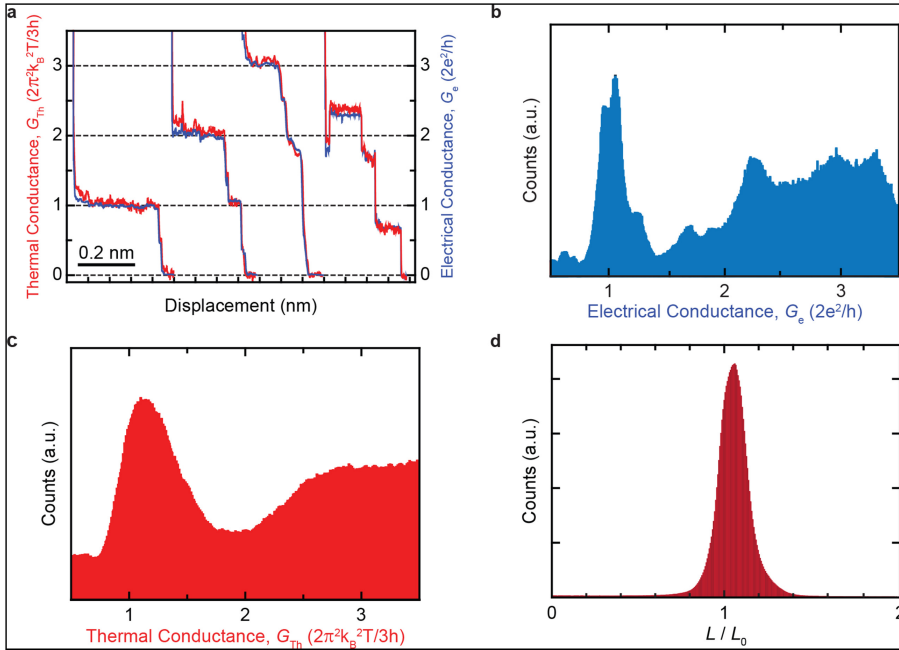


**Figure 8.3.** Experimentally measured quantized thermal transport in Au single-atom junctions. (a) Typical measured traces of thermal (red) and electrical (blue) conductances, in the units of  $2\pi^2k_B^2T/3h$  ( $2g_0$ , twice the thermal conductance quantum) and  $2e^2/h$  ( $G_0$ , the electrical conductance quantum), respectively. (b) and (c) Histograms of electrical and thermal conductances, obtained from 2000 consecutively measured conductance traces. (d) Analysis of the measured histograms of thermal and electrical conductances shows that the Wiedemann–Franz law is valid at the atomic scale to predict the thermal conductance of Au atomic junctions (the peak is at 1.06). Figure reproduced with permission from [29]. Copyright 2017 American Association for the Advancement of Science.

corresponding to the multiple integers of the quantized conductances ( $G_0 = 2e^2/h$  for electrical transport, and  $G_{0,\text{Th}} = 2g_0 = 2\pi^2k_B^2T/3h$  for thermal transport, where a factor of 2 comes from the spin degeneracy in electron transport). By combining  $\sim 2000$  consecutively obtained traces into the histogram of electrical and thermal conductance, clear peaks are observed at  $1G_0$  and  $1G_{0,\text{Th}}$ , which provide a definite proof of thermal transport quantization in single-atom junctions.

In order to robustly estimate the electrical conductance of the junctions, an unbiased statistical analysis was performed where histograms were constructed from several hundred traces. Such an analysis is motivated by the fact that the transport properties of atomic junctions are sensitive to the atomic-scale details of the geometries. Further motivation comes from the fact that previous studies [33–35] have shown that the presence of plateaus in conductance measurements is insufficient evidence of transport quantization.

It is to be noted that strong quantum confinement effects drive the energy level spacing in metallic atomic junctions enabling energy level spacing of a few electron

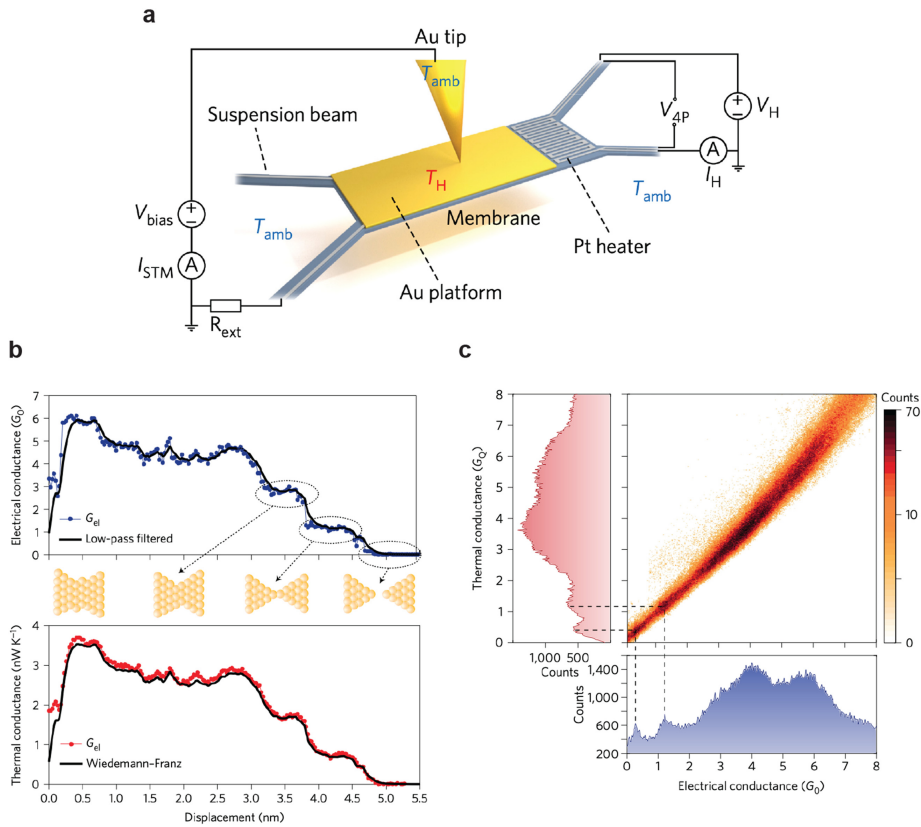


**Figure 8.4.** Experimental set-up for measuring heat transport in Au atomic junctions. (a) Schematics of the experimental set-up. (b) Measured electrical (upper panel) and thermal (lower panel) conductance trace, showing the stepwise behavior and the comparison with the prediction from the Wiedeman–Franz law. (c) Histograms of thermal and electrical conductances built from 2000 out of 5000 measured traces. Reproduced with permission from [36]. Copyright 2017 Macmillan Publishers.

volts, i.e. much larger than the thermal energy, making possible the above-described observations of quantized thermal transport at room temperature.

The developed C-SThM technique also makes it possible to investigate the validity of the Wiedemann–Franz law at the single-atom limit. The histogram in figure 8.4(d) illustrates the ratio of the measured thermal to electrical conductance, normalized by temperature and  $L_0$ ,  $G_{Th}/G_e T L_0$ . The Wiedemann–Franz law predicts this ratio to be equal to one and indeed it can be seen that the most probably value is very close to 1 ( $\sim 1.06$ ). According to the *ab initio* calculations performed for the Au single-atom junctions, the observed deviation ( $\sim 5\%$ – $10\%$ ) from the predicted value can be attributed to the phononic thermal conduction, which is small due to the mismatch of the vibrational energy spectrum between the atomic wire and the macroscopic electrodes.

In addition to the experiments described above, Mosso *et al* [36] have also studied heat transport across Au atomic-scale junctions using a different experimental

technique that is shown in figure 8.4. Briefly, they employed a suspended device with an integrated thermal sensor to measure the temperature change upon the rupture of an atomic junction, formed between an Au STM tip and an Au-coated region of the suspended device. Similar to the data shown in figure 8.3(a), they showed a strong correlation between the measured thermal and electrical conductance traces, which established a stepwise behavior during the breaking process of the atomic junctions (figure 8.4(b)). The Wiedemann–Franz law was also found to be valid at the atomic scale by applying a histogram analysis on both the thermal and electrical signals. Moreover, pronounced conductance peaks were observed at conductance values of  $0.4G_{0,\text{Th}}$  and  $1.3G_{0,\text{Th}}$ , rather than  $1G_{0,\text{Th}}$ , which is expected from the thermal conductance quantization in such atomic system [29]. This discrepancy was attributed to the potential existence of contaminant molecules (CO or H<sub>2</sub>O) absorbed on the Au membranes.

### 8.4 Heat dissipation in atomic- and molecular-scale junctions

To understand how heat is dissipated (the Joule effect) in atomic-sized junctions, Lee *et al* [37] developed an experimental approach that employed nanoscale thermocouple integrated scanning thermal microscope probes. In contrast to the C-SThM probes described above, these probes feature a sensitive nanoscale thermal sensor made of the Au–Cr junction (figure 8.5) which is located in close proximity to the apex of the tip. Multiple layers of dielectric and metallic thin films are deposited to form a sharp tip with a diameter of less than 300 nm.

In order to probe heat dissipation, an atomic or single-molecule junction is formed between the tip (coated with Au) and a flat Au substrate. A voltage bias ( $V$ ) applied across the junction leads to a temperature rise of the nanoscale thermocouple ( $\Delta T$ ) due to the energy dissipation. The temperature rise ( $\Delta T$ ) is related

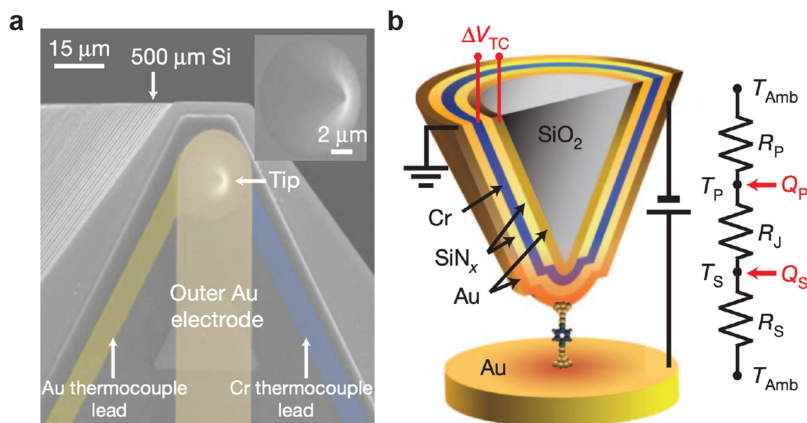


**Figure 8.5.** Experimental set-up for measuring heat dissipation in atomic-sized junctions. (a) SEM image of a nanoscale thermocouple integrated scanning thermal microscope probe. (b) Schematics of a single-molecule junction formed between the SThM tip (cross-sectional view) and a flat Au substrate. A thermal resistance network is shown on the right that represents the dominant thermal resistance to the dissipated heat flow. Figure reproduced with permission from [37]. Copyright 2013 Macmillan Publishers.

to the measured thermoelectric voltage ( $\Delta V_{TC}$ ) across the thermocouple by  $\Delta T = \Delta V_{TC}/S_{Au-Cr}$ , where  $S_{Au-Cr}$  is the Seebeck coefficient of the Au–Cr thermocouple. The heat dissipation ( $Q$ ) in the Au electrode of SThM probe can subsequently be quantified using  $Q = \Delta T/R_{probe}$ , where  $R_{probe}$  is the thermal resistance of the SThM probe.

This work revealed an intimate relationship between the heat dissipation and the electronic transmission characteristics of atomic-sized junctions. As summarized in figure 8.6, for single-molecule junctions that have transmission characteristics that are strongly energy-dependent, asymmetric heat dissipation was observed in the two electrodes between which the molecular junction is formed. Moreover, the heat dissipation was found to depend strongly on both the bias polarity and the identity of the majority charge carriers (electron- or hole-dominated transport in molecular junctions). In contrast, for Au atomic junctions, which have weak energy-dependent electronic transmission characteristics, the measured heat dissipation demonstrated no appreciable asymmetry. These observations, in conjunction with the first-principles calculations, provided the first experimental evidence that validates the use of the Landauer transport framework to understand heat dissipation in systems where elastic electron transport is dominant.

## 8.5 Peltier cooling in molecular-scale junctions

Current flow across molecular junctions results in both heat dissipation via the Joule effect and cooling via the Peltier effect. Net refrigeration can only be observed when the Peltier cooling power is larger in magnitude than Joule heating. To probe the

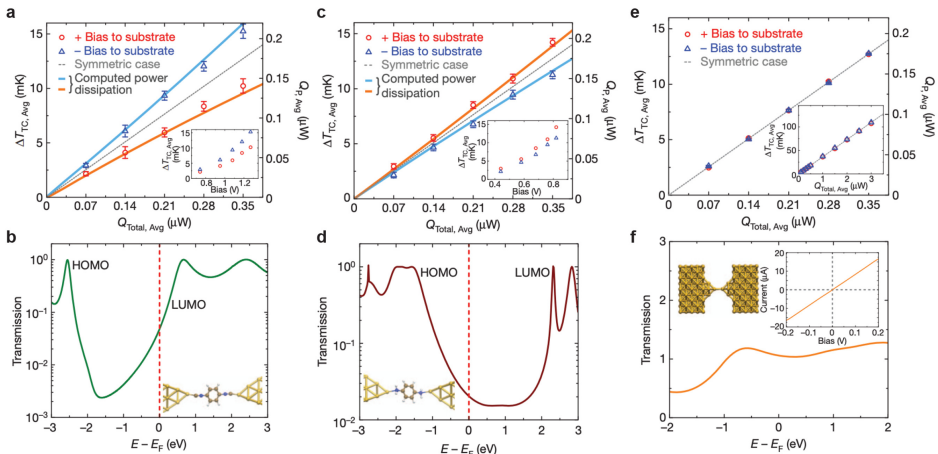


**Figure 8.6.** Measured heat dissipation in single-atom and single-molecule junctions. (a) Main panel, measured temperature rise of the thermocouple ( $\Delta T_{TC,Avg}$ ) and the power dissipation in the probe ( $Q_{P,Avg}$ ) as the function of the total power dissipation ( $Q_{Total,Avg}$ ) in the molecular junction (Au-BDNC-Au). Inset, measured temperature rise of the thermocouple as a function of the applied voltage bias. (b) Calculated zero-bias electronic transmission function of the BDNC junction. HOMO: highest occupied molecular orbital; LUMO: lowest unoccupied molecular orbital. Reproduced with permission from [37]. Copyright 2013 Macmillan Publishers.

cooling effect at the molecular scale, we developed an experimental platform, as illustrated in figure 8.7. Specifically, we custom-fabricated calorimetric microdevices with embedded high-resolution Pt thermometers that can resolve a temperature change as small as 0.1 mK [38]. The microdevices feature four long and doubly clamped  $\text{SiN}_x$  beams to achieve excellent thermal isolation. These characteristics enabled the measurement of heating and cooling power with  $\sim 30$  pW resolution.

During the measurement, a sharp Au-coated contact-mode AFM tip (with a radius of  $\sim 100$  nm) is used to make a soft contact with a monolayer of organic

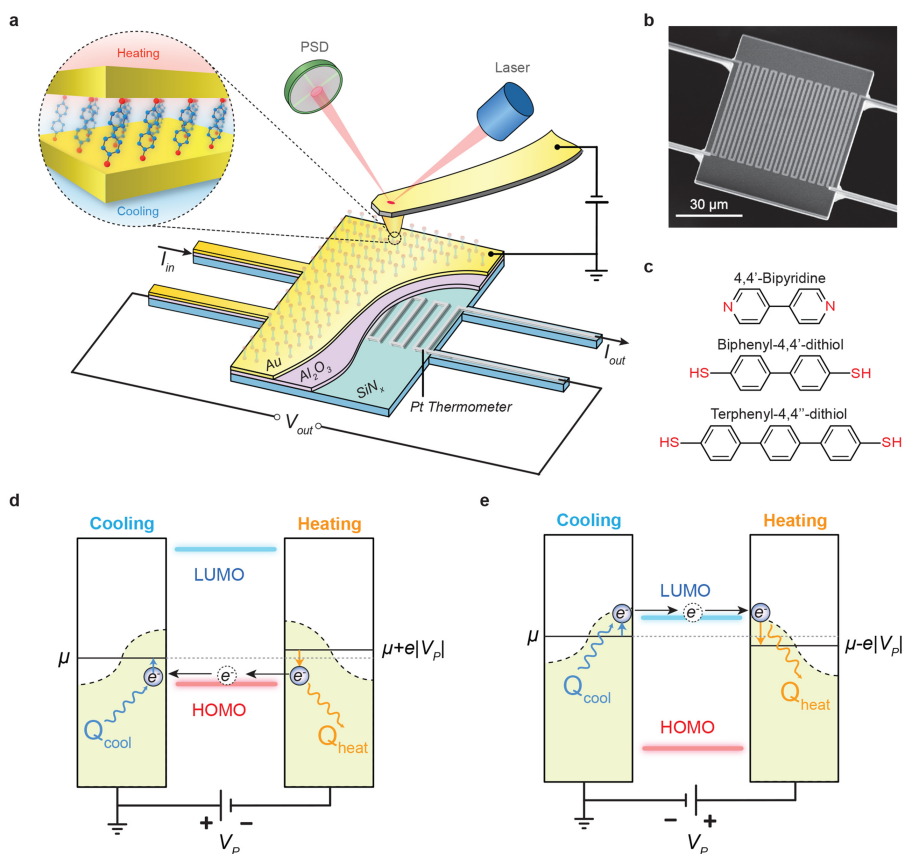


**Figure 8.7.** Experimental set-up of probing Peltier cooling in molecular junctions. (a) Schematic of the set-up. Molecular junctions are created by contacting an Au-coated atomic force microscope (AFM) tip with a monolayer of molecules self-assembled on an Au-coated calorimetric microdevice. The  $I$ - $V$  characteristic of molecular junctions is measured by supplying a small voltage bias across the junctions and monitoring the resultant electric current. The heating or cooling effect in the current-flowing molecular junctions is measured by recording the temperature change of the microdevices using the embedded Pt thermometer. (b) SEM image of the microdevice. (c) Chemical structures of the molecules studied including BP, BPDT and TPDT. (d)–(e) Description of the Peltier effect in a molecular junction in which transport is HOMO and LUMO-dominated, respectively. A Lorentzian shaped transmission function is depicted around the HOMO and LUMO levels of the molecular junctions.  $\mu_{cal}$ ,  $Q_{heat}$  and  $Q_{cool}$  denote chemical potential, heating and cooling power, respectively. Reproduced with permission from [38]. Copyright 2018 Macmillan Publishers.

molecules that are self-assembled on the top Au layer of the microdevice. It can be estimated that approximately 100 molecules are contained in the nanoscopic volume between the AFM tip and the substrate. A small voltage bias ( $<20$  mV) is applied across the molecular junctions to generate heating and cooling in the electrodes, which is captured on the side of the microdevice by the embedded Pt thermometer. The electrical conductance of the molecular junction can be quantified by measuring the resultant electrical current driven by the applied voltage bias, whereas the Seebeck coefficient of the molecular junctions could also be measured by applying suitable temperature differentials and probing the resulting thermoelectric voltage.

The observation of Peltier cooling in prototypical molecular junctions (Au–biphenyl-4,4'-dithiol (BPDT)–Au, Au–terphenyl-4,4''(TPDT)-dithiol–Au, and Au–4,4'-bipyridine (BP)–Au) is shown in figure 8.8. It can be seen that net refrigeration occurs within a narrow voltage interval at small biases. The maximum cooling power, observed in Au–BPDT–Au molecular junctions in this work, is around 300 pW for approximately 100 individual molecules. Depending on the identity of the majority charge carrier in the molecular junction, the voltage bias at which net refrigeration occurs can be either positive (for LUMO-dominated molecular junctions such as Au–BP–Au junctions) or negative (for HOMO-dominated molecular junctions such as Au–BPDT–Au and Au–TPDT–Au

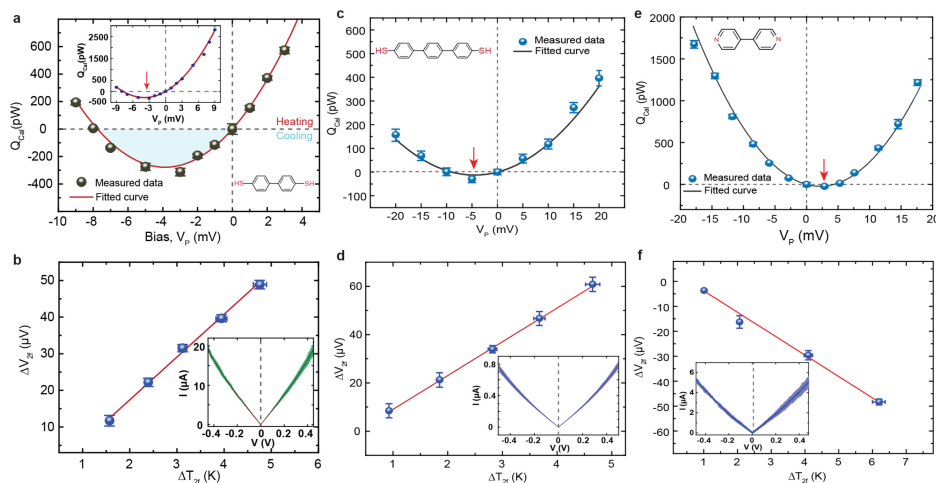


**Figure 8.8.** Measurement of the Peltier cooling, Seebeck effect and  $I$ - $V$  characteristic of molecular junctions. (a) Main panel: measured thermal power as the function of the applied voltage bias across the BPDT molecular junctions. The solid red line indicates the fitted curve using equation  $Q = Q_{\text{Pel}} + Q_{\text{Joule}} = GTSV + GV^2/2$  and the measured Seebeck coefficient and electrical conductance. The shaded blue region indicates the voltage region where net refrigeration is measured. Inset: the measured data and the fitted curve for voltage bias from  $-9$  to  $9$  mV. The red arrow indicates the voltage at which the maximum cooling is observed. (b) Measured Seebeck coefficient ( $S$ ) of the BPDT junctions. The red solid line indicates the best linear fit, with the slope showing the Seebeck coefficient. Inset: the  $I$ - $V$  characteristics of the junctions. (c) and (e) The same as (a), but for TPDT and BP molecular junctions, respectively. (d) and (f) The same as (b), but for TPDT and BP molecular junctions, respectively. Reproduced with permission from [38]. Copyright 2018 Macmillan Publishers.

junctions). The parabolic shape of the heating or cooling power versus voltage bias curve can be understood readily in the Landauer transport framework (section 8.2.2), that is, in the small bias limit the total heating or cooling power of the molecular junction is the summation of the Peltier effect ( $Q_{\text{Pel}} = GTSV$ ) and the Joule effect ( $Q_{\text{Joule}} = GV^2/2$ ), where  $G$  is the electrical conductance,  $S$  is the Seebeck coefficient,  $V$  is the applied bias and  $T$  is the absolute temperature. As described above, our developed platform is capable of characterizing multiple transport parameters including electrical conductance and the Seebeck coefficient. Further experimental investigations have demonstrated the remarkable consistency between the measured heating and cooling power and the predictions of the Landauer framework.

## 8.6 Measurement of thermal conductance of single-molecule junctions

The study of heat transport in single-molecule junctions offers unique opportunities to reveal the fundamental mechanisms of vibrational (phonon) energy transport. Unlike heat transport in macroscopic and most mesoscopic materials where incoherent phonons govern the energy processes, thermal phonons in short molecule junctions transport coherently, even at room temperature. Peculiar phenomena are expected to arise, such as quantum interference of thermal transport [39]. Moreover, as natural one-dimensional physical systems, individual molecules may help provide deep insight into understanding the Fermi–Pasta–Ulam problem [40], an over half-century-old research topic regarding the possibility of anomalous infinitely large thermal conductivity in one-dimensional systems.

As a first step in the understanding of heat transfer at the single-molecule scale, our recent experimental study [41] has measured the thermal conductance of a series of single alkanedithiol molecule junctions and revealed the dependence of thermal transport on the number of molecular units. Specifically, we leveraged the scanning thermal microscopy SThM set-up (figure 8.9(a)) developed to measure the quantized thermal transport in single metallic-atom junctions. Once a molecule junction is trapped between the SThM tip and the substrate, the pre-applied temperature and voltage bias differential will allow both the heat current and electrical current flowing through the molecule junction. Figure 8.9(b) shows the measured electrical conductance and thermal conductance traces of a single hexanedithiol (C6) junction right before and after the spontaneous junction rupture. It can be seen that while the electrical signal exhibited a sudden drop by  $\sim 6 \times 10^{-4} G_0$  indicating the existence of a single-molecule junction, a corresponding conductance change is not discernible in the simultaneously recorded thermal signal. To improve the signal-to-noise ratio of thermal measurement, we implemented a time-averaging scheme by first performing hundreds of electrical and thermal measurements and then using the electrical conductance versus time traces to identify the time point when the junction rupture occurs. Using the electrical conductance signals as references, we then aligned and averaged the measured thermal signal to obtain a time-averaged thermal conductance curve. In figure 8.9(c), the results of thermal conductance after averages over

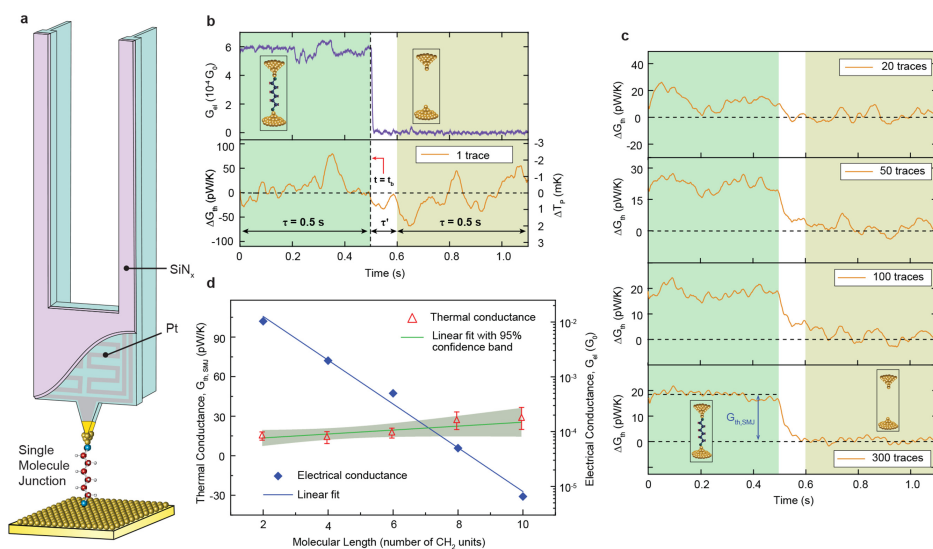


**Figure 8.9.** Measurements of the thermal conductance of single-molecule junctions. (a) Schematics of a single molecule trapped between an Au-coated tip of the heated SThM probe and an Au substrate at room temperature. The thermal conductance of single-molecule junctions is quantified by recording the temperature change of the Pt heater-thermometer when a single-molecule junction is broken. (b) Experimental protocol for measuring the thermal conductance of a single hexanedithiol (C6) junction. Upper panel: measured single electrical conductance versus time trace showing junction rupture at  $t = t_b$ , accompanied by a sudden drop of the conductance value. Lower panel: the simultaneously measured thermal conductance change ( $\Delta G_{th}$ ) and temperature change ( $\Delta T_p$ ) showing a large noise background in which the expected thermal conductance change is buried. (c) Improvement of the signal-to-noise ratio is clearly seen from the time-averaging of 20, 50, 100 and 300 traces.  $G_{th,SMJ}$  in the last panel indicates the measured thermal conductance of Au-C6-Au single-molecule junctions. (d) Length-dependent electrical (blue diamonds) and thermal conductance (red triangles) of single alkanedithiol molecule junction. Reproduced with permission from [41]. Copyright 2019 Macmillan Publishers.

20, 50, 100 and 300 traces are illustrated, and reveal a clear thermal conductance jump at the time point when the junction ruptures.

Following the same experimental protocol, we have studied a series of alkanedithiol molecule junctions with different molecular units ( $-\text{CH}_2$ , from 2 to 10). As shown in figure 8.9(d), the measured electrical conductance exhibits an exponentially decaying behavior, as expected from the tunneling electron transport-dominated mechanism in such junctions. However, the thermal conductance of alkanedithiol molecules with different molecular lengths is observed to be nearly constant at a value of approximately  $20 \text{ pW K}^{-1}$ , strongly suggesting that phonon transport in these junctions is ballistic. We have also performed first-principles calculations which provide strong support for the experimental observations and detailed mechanisms in terms of the coherent vibrational energy transport in the single-molecule junctions.

## 8.7 Concluding remarks and outlook

Recently developed high-resolution scanning thermal microscopy techniques have made significant progress in probing energy transport in atomic-sized structures and testing the limitations of existing theoretical frameworks. These techniques and approaches set the stage for exploration of thermal and electrical properties of a broad range of atomic- and nano-structures and materials. Below, we briefly highlight some of the open questions in the field of atomic- and molecular-scale thermal science and, in light of the recent experimental advancements, we believe the first sets of measurements to address these open challenges are possible in the near future and would provide important insight into our current understanding of energy processes at the fundamental limit.

A central challenge in the field of thermoelectrics is to search for materials with a high thermoelectric figure of merit  $ZT$ . Bismuth telluride, the mostly applied thermoelectric material, possesses a  $ZT$  of  $\sim 1$ , corresponding to  $< 20\%$  of Carnot efficiency in energy conversion applications. This is significantly lower than the thermodynamic efficiency of energy conversion technologies such as internal combustion engines. A  $ZT > 3$  is considered favorable to compete with traditional technologies, in particular at or slightly above room temperature. One fundamental question that remains to be answered in molecular systems is how high a value of  $ZT$  can be achieved in principle. Recent theoretical studies [42–47] have predicted high  $ZT$  values in specifically designed or synthesized molecular junctions due to quantum effects that have no classical analogues. One may ask, can we design proper experiments to validate these theoretical proposals? How can we rationally design the chemical structure of molecules to selectively enhance favorable transport properties and simultaneously suppress others for thermoelectric applications?

Another open question is to deepen our understanding of thermal (specifically phonons) transport in one-dimensional molecular systems such as individual polymer chains. Although previous experimental efforts [48–57] were made to characterize thermal transport in ensembles of molecules, such as self-assembled monolayers and polymer nanofibers, the recent study of single-molecule junctions allows one to resolve the issue of ensemble-based molecular measurements, such as uncertainties due to the heterogeneities of the molecules as well as potential influences of intermolecular interactions [58]. We expect that systematic experimental studies of single-molecule heat transport will enable comparisons among competing theories and help set the design principles for organic molecules for optimal thermal transport in soft materials.

## References

- [1] Agrait N, Yeyati A L and van Ruitenbeek J M 2003 *Phys. Rep.* **377** 81–279
- [2] Aradhya S V and Venkataraman L 2013 *Nat. Nanotechnol.* **8** 399–410
- [3] Imry Y 1997 *Introduction to Mesoscopic Physics* (New York: Oxford University Press), p xiii
- [4] Landauer R 1957 *IBM J. Res. Dev.* **1** 223–31
- [5] Landauer R 1989 *J. Phys. Condens. Mater.* **1** 8099–110

- [6] Datta S 2005 *Quantum Transport: Atom to Transistor* (Cambridge: Cambridge University Press) p xiv
- [7] Cuevas J C and Scheer E *Molecular Electronics: An Introduction to Theory and Experiment* Q1 p xix
- [8] Esfarjani K, Zebarjadi M and Kawazoe Y 2006 *Phys. Rev. B* **73** 085406
- [9] Chiatti O, Nicholls J T, Proskuryakov Y Y, Lumpkin N, Farrer I and Ritchie D A 2006 *Phys. Rev. Lett.* **97** 056601
- [10] Jezouin S, Parmentier F D, Anthore A, Gennser U, Cavanna A, Jin Y and Pierre F 2013 *Science* **342** 601–4
- [11] Meschke M, Guichard W and Pekola J P 2006 *Nature* **444** 187–90
- [12] Partanen M, Tan K Y, Govenius J, Lake R E, Makela M K, Tanttut T and Mottonen M 2016 *Nat. Phys.* **12** 460–4
- [13] Schwab K, Henriksen E A, Worlock J M and Roukes M L 2000 *Nature* **404** 974–7
- [14] Ashcroft N W and Mermin N D 1976 *Solid State Physics* (New York: Holt) p xxi
- [15] Crossno J *et al* 2016 *Science* **351** 1058–61
- [16] Wakeham N, Bangura A F, Xu X, Mercure J F, Greenblatt M and Hussey N E 2011 *Nat. Commun.* **2** 396
- [17] Sivan U and Imry Y 1986 *Phys. Rev. B* **33** 551–8
- [18] Lake R and Datta S 1992 *Phys. Rev. B* **46** 4757–63
- [19] Butcher P N 1990 *J. Phys. Condens. Mat.* **2** 4869–78
- [20] Paulsson M and Datta S 2003 *Phys. Rev. B* **67** 241403
- [21] Cahill D G 2004 *Rev. Sci. Instrum.* **75** 5119–22
- [22] Balandin A A 2011 *Nat. Mater.* **10** 569–81
- [23] Majumdar A 1999 *Annu. Rev. Mater. Sci.* **29** 505–85
- [24] Kim K, Jeong W H, Lee W C and Reddy P 2012 *ACS Nano* **6** 4248–57
- [25] Menges F, Mensch P, Schmid H, Riel H, Stemmer A and Gotsmann B 2016 *Nat. Commun.* **7** 10874
- [26] Cui L, Jeong W, Fernandez-Hurtado V, Feist J, Garcia-Vidal F J, Cuevas J C, Meyhofer E and Reddy P 2018 *Nat. Commun.* **9** 14479
- [27] Jeong W, Hur S, Meyhofer E and Reddy P 2015 *Nanoscale Microsc. Therm.* **19** 279–302
- [28] Cui L, Miao R, Jiang C, Meyhofer E and Reddy P 2017 *J. Chem. Phys.* **146** 092201
- [29] Cui L, Jeong W, Hur S, Matt M, Klockner J C, Pauly F, Nielaba P, Cuevas J C, Meyhofer E and Reddy P 2017 *Science* **355** 1192–5
- [30] Yanson A I, Bollinger G R, van den Brom H E, Agrait N and van Ruitenbeek J M 1998 *Nature* **395** 783–5
- [31] Scheer E, Agrait N, Cuevas J C, Yeyati A L, Ludoph B, Martin-Rodero A, Bollinger G R, van Ruitenbeek J M and Urbina C 1998 *Nature* **394** 154–7
- [32] Xu B Q and Tao N J J 2003 *Science* **301** 1221–3
- [33] Olesen L, Laegsgaard E, Stensgaard I, Besenbacher F, Schiøtz J, Stoltze P, Jacobsen K W and Nørskov J K 1994 *Phys. Rev. Lett.* **72** 2251–4
- [34] Krans J M, Muller C J, Vanderpost N, Postma F R, Sutton A P, Todorov T N and Vanruitenbeek J M 1995 *Phys. Rev. Lett.* **74** 2146
- [35] Olesen L, Laegsgaard E, Stensgaard I, Besenbacher F, Schiøtz J, Stoltze P, Jacobsen K W and Nørskov J K 1995 *Phys. Rev. Lett.* **74** 2147
- [36] Mosso N, Drechsler U, Menges F, Nirmalraj P, Karg S, Riel H and Gotsmann B 2017 *Nat. Nanotechnol.* **12** 430–3

- [37] Lee W, Kim K, Jeong W, Zotti L A, Pauly F, Cuevas J C and Reddy P 2013 *Nature* **498** 209–13
- [38] Cui L, Miao R, Wang K, Thompson D, Zotti L A, Cuevas J C, Meyhofer E and Reddy P 2018 *Nat. Nanotechnol.* **13** 122–7
- [39] Markussen T 2013 *J. Chem. Phys.* **139** 244101
- [40] Fermi E, Pasta J and Ulam S 1955 Los Alamos Report, LA-1940 978
- [41] Cui L, Hur S, Akbar Z A, Klockner J C, Jeong W, Pauly F, Jang S Y, Reddy P and Meyhofer E 2019 *Nature* **572** 628–33
- [42] Murphy P, Mukerjee S and Moore J 2008 *Phys. Rev. B* **78** 161406
- [43] Sadeghi H, Sangtarash S and Lambert C J 2015 *Nano Lett.* **15** 7467–72
- [44] Karlstrom O, Linke H, Karlstrom G and Wacker A 2011 *Phys. Rev. B* **84** 113415
- [45] Bergfield J P, Solis M A and Stafford C A 2010 *ACS Nano* **4** 5314–20
- [46] Finch C M, Garcia-Suarez V M and Lambert C J 2009 *Phys. Rev. B* **79** 033405
- [47] Hou S J, Wu Q Q, Sadeghi H and Lambert C J 2019 *Nanoscale* **11** 3567–73
- [48] Xu Y F, Wang X X, Zhou J W, Song B, Jiang Z, Lee E M Y, Huberman S, Gleason K K and Chen G 2018 *Sci. Adv.* **4** eaar3031
- [49] Wang X J, Ho V, Segalman R A and Cahill D G 2013 *Macromolecules* **46** 4937–43
- [50] Meier T, Menges F, Nirmalraj P, Holscher H, Riel H and Gotsmann B 2014 *Phys. Rev. Lett.* **113** 060801
- [51] Shen S, Henry A, Tong J, Zheng R T and Chen G 2010 *Nat. Nanotechnol.* **5** 251–5
- [52] Wang R Y, Segalman R A and Majumdar A 2006 *Appl. Phys. Lett.* **89** 173113
- [53] Wang Z H, Carter J A, Lagutchev A, Koh Y K, Seong N H, Cahill D G and Dlott D D 2007 *Science* **317** 787–90
- [54] Losego M D, Grady M E, Sottos N R, Cahill D G and Braun P V 2012 *Nat. Mater.* **11** 502–6
- [55] Majumdar S, Sierra-Suarez J A, Schiffres S N, Ong W L, Higgs C F, McGaughey A J H and Malen J A 2015 *Nano Lett.* **15** 2985–91
- [56] Ge Z B, Cahill D G and Braun P V 2006 *Phys. Rev. Lett.* **96** 186101
- [57] O'Brien P J, Shenogin S, Liu J X, Chow P K, Laurencin D, Mutin P H, Yamaguchi M, Koblinski P and Ramanath G 2013 *Nat. Mater.* **12** 118–22
- [58] Majumdar S, Malen J A and McGaughey A J H 2017 *Nano Lett.* **17** 220–7